A FINITE ELEMENT TEST BED FOR DIFFRACTION TOMOGRAPHY

Z. You and W. Lord

Department of Electrical Engineering and Computer Engineering
Iowa State University
Ames, Iowa 50011

INTRODUCTION

Finite element analysis methods have been successfully applied to the study of ultrasonic wave propagation in elastic solids [1-4]. As a natural part of such numerical solutions, displacements are predicted for every node of the spatial discretization describing the solids geometry and at every instant of time in the temporal discretization used to define the pulse propagation through the material. All of the data constitute a solution to the forward problem and can be used to visualize wavefront propagation and interactions with defects, thus predicting displacement signals at any point in or on the solid.

Inverse algorithms, on the other hand, extract information about the geometric structure or contour of the interior parameters of a scatterer in a homogeneous environment from the wave-field obtained on the measurement surface. For diffraction sources such as ultrasound, the inverse scheme should be based on the wave equation rather than on the assumption of a straight line path from the source to the receiver as in X-ray tomography [5-6]. Based on the Born or Rytov approximation [7], diffraction tomography reconstructs the object function from the planar measurement of the displacement field by back-propagating the displacement to the full-space and summing over the frequency or over the different angles [8-10].

The data from finite element simulations of the forward problem can serve as raw data for input to inverse algorithms. Since it is easy to change the material parameters, shape of the scatterer, source signal and aperture size, the finite element code provides an effective test bed on which the sensitivity of reconstruction techniques can be studied subject to a wide variety of test variables.

Only isotropic materials are considered here. Through the Helmholtz decomposition, the elastic wave equation results in the Helmholtz equations. This paper, therefore, derives the diffraction tomographic algorithm from the scalar wave equation in 2-D geometries.

RECONSTRUCTION ALGORITHM

For a scatterer located in the $z < 0$ space, the scattered wave in the $z \geq 0$ space satisfies the 2-D homogeneous wave equation

Review of Progress in Quantitative Nondestructive Evaluation, Vol. 9
Edited by D.O. Thompson and D.E. Chimenti
Plenum Press, New York, 1990

$$\nabla^2 \phi + k_0^2 \phi = 0 \tag{1}$$

where k_0 is the wave number of the host material.

A 1-D Fourier transformation of Eq. (1) with respect to y gives the following migration relationship

$$\hat{\phi}(k_y, z; \omega) = \hat{\phi}(k_y, z = 0; \omega) e^{j\sqrt{k_0^2 - k_y^2}\, z} \tag{2}$$

which propagates the wave in the $z = 0$ line to any $z > 0$ line.

For a penetrable scatterer, the total field should satisfy the following inhomogeneous equation [9]

$$\nabla^2 \phi + k_0^2 \phi = -O(\underline{r}) k_0^2 \phi \tag{3}$$

where $O(\underline{r}) = \left| 1 - \dfrac{k^2(\underline{r})}{k_0^2} \right|$ is the object function which is zero outside the scatterer, and $k(\underline{r})$ is the wave number defined for all space.

The left-hand side of Eq. (3) is equivalent to a secondary source for the scattered wave field

$$q_c = -O(\underline{r}) k_0^2 \phi(\underline{r}) \tag{4}$$

Let C_M represent an arbitrary measurement curve enclosing an area of A_M. Define a generalized holographic field $\phi_H(\underline{r}, \omega)$ in terms of the Huygen-type back-propagation principle [8]

$$\phi_H(\underline{r}, \omega) = -\int_{C_M} \left[\phi_s(\underline{r}, \omega) \frac{\partial G^*}{\partial n'} - G^*(\underline{r} - \underline{r}', \omega) \frac{\partial \phi_s}{\partial n'} \right] dl \tag{5}$$

where G^* is the complex conjugate of the 2-D free-space Green's function and n' is the outward normal to C_M. This expression is valid only for $\underline{r} \in A_M$. Further manipulation yields the so-called Porter-Bojarski integral equation [11]

$$\phi_H(\underline{r}, \omega) = 2j \int\int_{A_M} q_c(\underline{r}', \omega) G_i(\underline{r} - \underline{r}', \omega) d^2 \underline{r} \tag{6}$$

where G_i is the imaginary part of the free-space Green's function. Fourier transformation of this equation yields

$$\tilde{\phi}_H(\underline{K}, \omega) = 2j\, \tilde{q}_c(\underline{K}, \omega) \tilde{G}_i(\underline{K}, \omega) \tag{7}$$

In 2-D geometry, it can be shown that

$$G_i(\underline{r} - \underline{r}', \omega) = \frac{1}{4} J_0(k\, |\underline{r} - \underline{r}'|) \tag{8}$$

where J_0 is the zeroth order Bessel function of the first kind. Fourier transformation of the Bessel function yields

$$\tilde{G}_i(\underline{K}, \omega) = \frac{\pi}{2} \frac{\delta(K - k)}{K} \tag{9}$$

where $K = |\underline{K}|$.

Consider weak scattering cases. For an incident plane wave, the Born approximation relates the secondary source to the object function by [8]

$$q_c^{Born}(\underline{r}, \theta_i, \omega) = k^2 O(\underline{r}) F(\omega) e^{j\underline{k}_i(\theta_i, \omega) \cdot \underline{r}} \tag{10}$$

where θ_i is the incident angle (Fig. 1), $\underline{k}_i = (-\cos\theta_i, -\sin\theta_i)$, $\underline{r} = (x, z)$, and $F(\omega)$ is the frequency dependency of the incident field.

Fourier transforming this equation yields

$$\tilde{q}_c(\underline{K}, \omega) = -k^2 F(\omega) \tilde{O}(\underline{K} - \underline{k}_i) \tag{11}$$

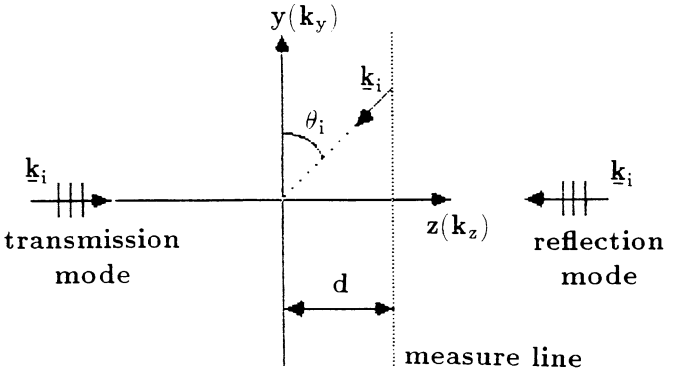

Fig. 1. Illustration of the incident direction.

Substitute Eqs. (9) and (11) into Eq. (7) produces

$$\tilde{\phi}_H(\underline{K}+\underline{k}_i,\omega) = -j\pi kF(\omega)\tilde{O}(\underline{K})\delta(|\underline{K}+\underline{k}_i|-k) \tag{12}$$

For planar measurements, the space is only defined in the interval $[0,\pi]$ instead of $[0,2\pi]$ for full space. That is

$$\tilde{\phi}_H(\underline{K}+\underline{k}_i,\omega) = -j\pi kF(\omega)\tilde{O}(\underline{K})u(k_z-k\sin\theta_i)\delta(|\underline{K}+\underline{k}_i|-k) \tag{13}$$

where u is a unit step function.

Consider the reflection mode. Fig. 1 gives $\theta_i = \frac{\pi}{2}$, $\underline{k}_i = k(0,-1)$. Eq. (13), therefore, results in

$$\frac{1}{\pi}\frac{j}{k^3F(\omega)}\tilde{\phi}_H(k_y,k_z-k,\omega) = \frac{\tilde{O}(\underline{K})}{k^2}u(k_z-k)\delta\left(\sqrt{k_y^2+(k_z-k)^2}-k\right) \tag{14}$$

Integrating both sides yields

$$\frac{1}{\pi}\int_0^\infty \frac{j}{k^3F(\omega)}\tilde{\phi}_H(k_y,k_z-k,\omega)dk = \tilde{O}(\underline{K})I_{TM}(\underline{K}) \tag{15}$$

where

$$\begin{aligned} I_{TM}(\underline{K}) &= \int_0^\infty \frac{1}{k^2}\delta\left(\sqrt{k_y^2+(k_z-k)^2}-k\right)u(k_z-k)dk \\ &= \frac{2}{K^2}u(k_z)u(k_z-|k_y|) \end{aligned} \tag{16}$$

and $\tilde{\phi}_H$ can be represented as

$$\tilde{\phi}_H(k_y,k_z-k,\omega) = \int_{-\infty}^{\infty}\hat{\phi}_H(k_y,z,\omega)e^{-j(k_z-k)z}dz \tag{17}$$

while $\hat{\phi}_H(k_y,z,\omega)$ can be related to the back-propagation of the measured wavefield at $z = d$ line, i.e.

$$\hat{\phi}_H(k_y,z,\omega) = \hat{\phi}_M(k_y,z=d,\omega)e^{j(z-d)\sqrt{k^2-k_y^2}} \tag{18}$$

Therefore

$$\begin{aligned} \tilde{O}(\underline{K})u(k_z)u(k_z-|k_y|) = \frac{1}{2\pi}j\int_0^\infty \frac{k+\sqrt{k^2-k_y^2}}{k^2F(\omega)}\delta\left(k_z-k-\sqrt{k^2-k_y^2}\right) \\ \hat{\phi}_M(k_y,z=d,\omega)e^{-jd\sqrt{k^2-k_y^2}}u(k^2-k_y^2)dk \end{aligned} \tag{19}$$

Since the product of the step functions in the left-hand side cannot be inverse Fourier transformed, we define a spatially filtered object function by Fourier inverse transformation of the right-hand side as

$$O_{\Lambda P}(\underline{r}) = \frac{j}{(2\pi)^3}\int_0^{\infty}\frac{dk}{k^2F(\omega)}\int_{-\infty}^{\infty}\left[k+\sqrt{k^2-k_y^2}\right]\phi_M(k_y, z=d, \omega)$$
$$e^{-jkz}e^{j(z-d)\sqrt{k^2-k_y^2}}u(k^2-k_y^2)e^{jk_y y}\,dk_y \qquad (20)$$

where Λ is the shape of the filter $u(k_z)u(k_z-|k_y|)$.

For transmission mode, $\theta_i = \frac{3\pi}{2}$, $k_i = k(0,1)$ as shown in Fig. 1. Similar processes yield

$$O_{\Sigma P}(\underline{r}) = \frac{j}{(2\pi)^3}\int_0^{\infty}\frac{dk}{k^2F(\omega)}\int_{-\infty}^{\infty}\left[k-\sqrt{k^2-k_y^2}\right]\phi_M(k_y, z=d, \omega)$$
$$e^{-jkz}e^{j(z-d)\sqrt{k^2-k_y^2}}u(k^2-k_y^2)e^{jk_y y}\,dk_y \qquad (21)$$

where Σ represents the shape of the filter $u(-k_z)u(k_z+|k_y|)$ involved in the derivations.

Eqs. (20) and (21) are the reconstruction algorithms used throughout the rest of the paper.

RAW DATA GENERATION

Instead of measuring experimental data, finite element code [4] is used here to provide the raw data for exercising different tomographic algorithms as derived in the previous section. An aluminum block, having a longitudinal velocity $v_L = 6300m/s$, a shear velocity $v_S = 3100m/s$ and density $\rho = 2700kg/m^3$, contains a small crack which is illuminated by a longitudinal plane wave. The reflected wave from the crack is sensed on the front wall of the block, while the transmitted wave is recorded on the back wall. A typical displacement slice at t = $10\mu s$ is shown in Fig. 2 along with the geometry.

The second example is a similar aluminum block containing two cracks. The displacement field at t = $8\mu s$ is shown in Fig. 3.

There are 65,025 rectangular elements used in the computation. The number of time steps is 512 with an increment of $40ns$. The total CPU-time required for this simulation is 28.1 minutes on the NAS AS/9160 computer system.

RECONSTRUCTED IMAGE

Fourier transformation of the z-displacement on the front wall with respect to time t provides the measured data $\phi_M(x, z=0, \omega)$ in the frequency domain. Further Fourier transformation of the ϕ_M with respect to x gives $\phi_M(k_x, z=0, \omega)$ as required in Eq. (20). The reconstructed image by the frequency diversity diffraction tomographic algorithm in reflection mode (Eq. (20)) is shown in Fig. 4. This image shows good agreement with the original crack as illustrated in Fig. 2. The same algorithm is also used to reconstruct the two cracks in Fig. 3. The resulted image is shown in Fig. 5. The data received on the back wall are used with the transmission mode (Eq. (21)) in the same way as described before for the reflection mode. The reconstructed two-crack image is shown in Fig. 6. This image does not give the correct information about the different depths of these two cracks. The explanation is that the transmitted data does not have the information about the depths of the cracks. The depths, however, are related to the arrival

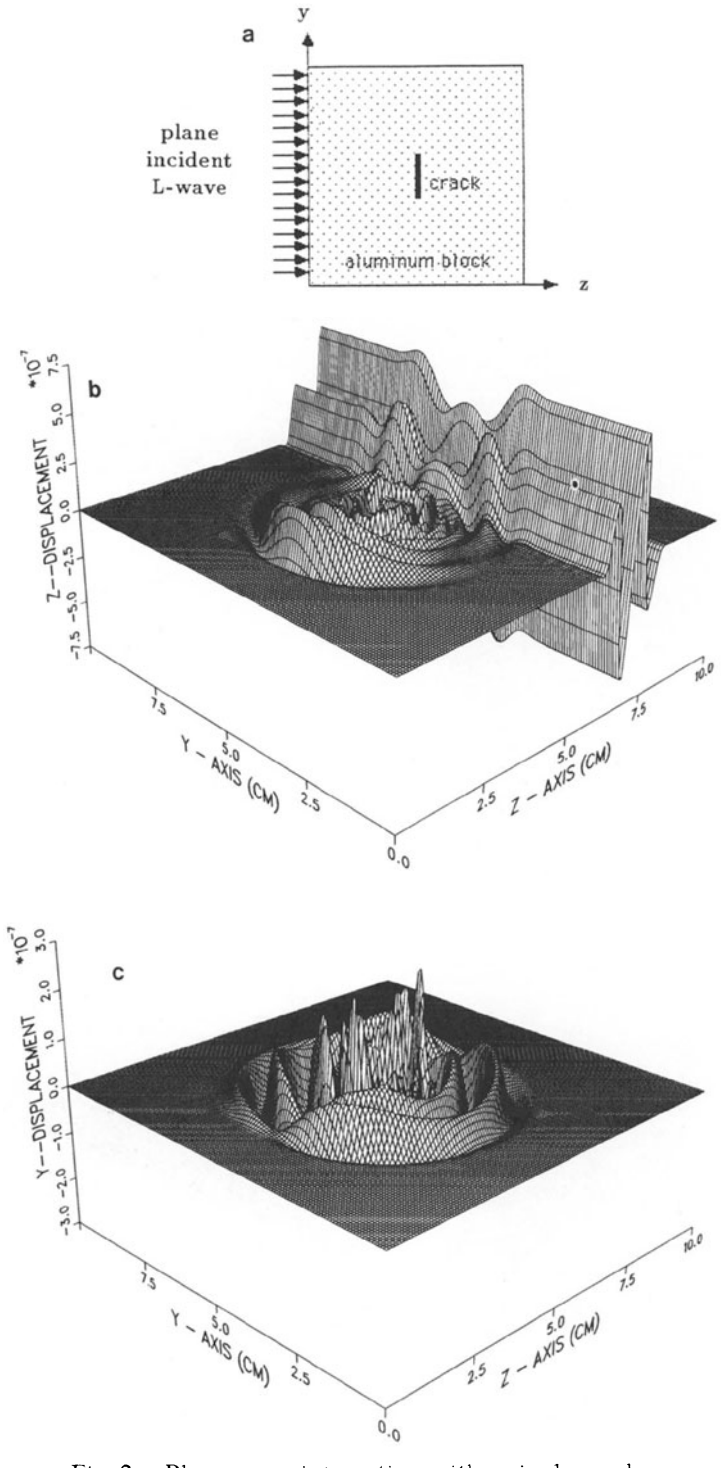

Fig. 2. Plane wave interaction with a single crack.
a) geometry detail.
b) z-displacement at $t = 10\mu s$.
c) y-displacement at $t = 10\mu s$.

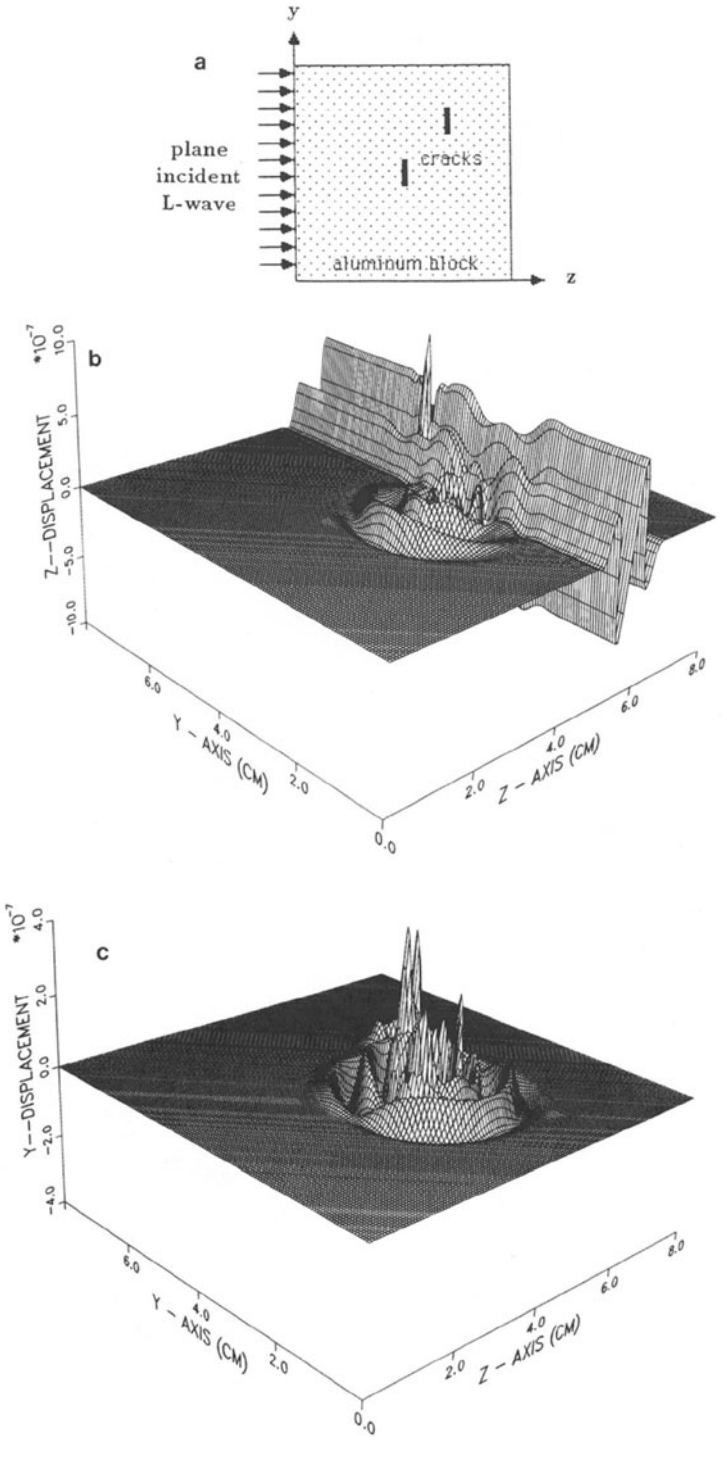

Fig. 3. Plane wave interaction with two single crack.
a) geometry detail.
b) z-displacement at $t = 8\mu s$.
c) y-displacement at $t = 8\mu s$.

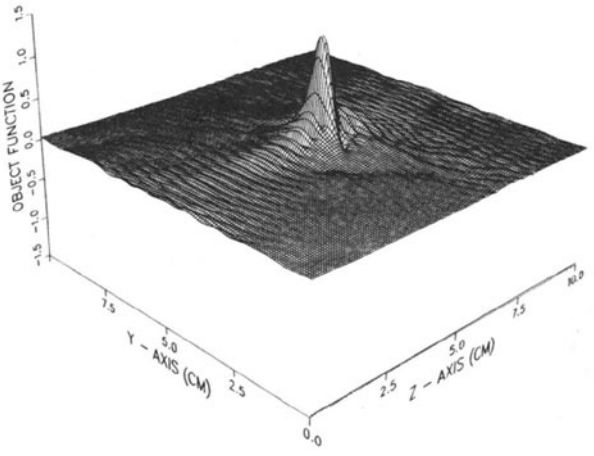

Fig. 4. Reconstructed image of Fig. 2a by Eq. (20).

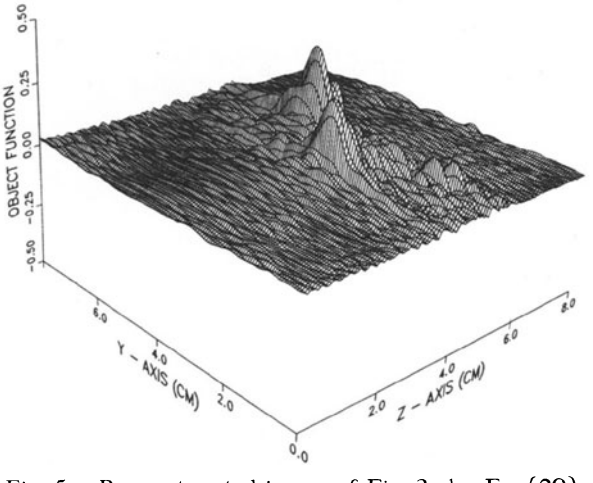

Fig. 5. Reconstructed image of Fig. 3a by Eq. (20).

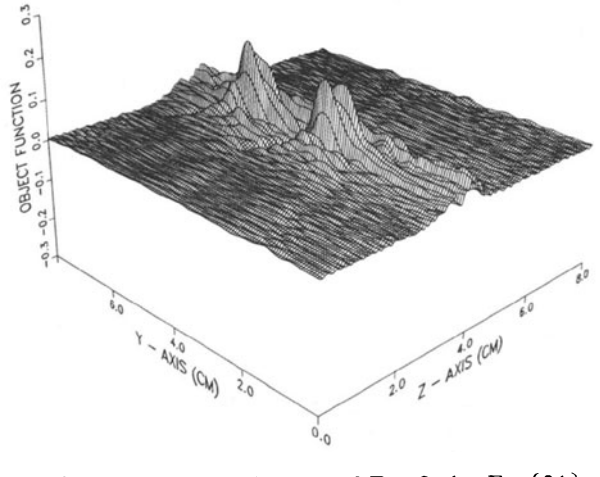

Fig. 6. Reconstructed image of Fig. 3a by Eq. (21).

time of the reflected data. This is one of the advantages of the reflection mode over the transmission mode. The reflection mode also has a better resolution than that of the transmission mode because of the better space coverage of the Λ-shaped filter than the $\sum$-shaped filter for a finite bandwidth source signal.

In the case of a strong scatterer, diffraction tomography cannot reconstruct the object function for a volumetric defect. The reconstructed image only gives the contour of the illuminated side of the defect.

CONCLUSIONS

Frequency diversity diffraction tomographic algorithms in the reflection mode perform better than in transmission mode. Weak scatterer approximations do reconstruct the illuminated edge for the strong scatterer. Finite element simulation can be an effective test bed for inverse algorithms because all needed data for a variety of test variables can be easily obtained.

REFERENCES

1. R. Ludwig and W. Lord, "A Finite Element Formulation for Ultrasonic NDT Modeling," in Review of Progress in Quantitative NDE, edited by D. O. Thompson and D. E. Chimenti (Plenum Press, New York, 1985), Vol. 4A, p. 37.
2. R. Ludwig and W. Lord, "Development in the Finite Element Modeling of Ultrasonic NDT Phenomena," in Review of Progress in Quantitative NDE, edited by D. O. Thompson and D. E. Chimenti (Plenum Press, New York, 1986), Vol. 5A, p. 73.
3. Z. You, W. Lord and R. Ludwig, "Numerical Modeling of Elastic Wave Propagation in Anisotropic Materials," Review of Progress in Quantitative NDE, edited by D. O. Thompson and D. E. Chimenti (Plenum Press, New York, 1988), Vol. 7A, p. 23.
4. Z. You and W. Lord, "Finite Element Study of Elastic Wave Interaction with Cracks," Review of Progress in Quantitative NDE, edited by D. O. Thompson and D. E. Chimenti (Plenum Press, New York, 1989), Vol. 8A, p. 109.
5. G. T. Herman, Image Reconstruction from Projections: The Fundamentals of Computerized Tomography, (Academic Press, New York, 1980).
6. R. K. Mueller, M. Kaveh and G. Wade, "Reconstructive Tomography and Application to Ultrasonics," Proceedings of IEEE, Vol. 167, p. 567 (1979).
7. M. Kaveh, M. Soumekh and R. K. Mueller, "A Comparison of Born and Rytov Approximation in Acoustic Tomography," Acoustical Imaging, Vol. 11, p. 325 (1981).
8. K. J. Langenberg, "Applied Inverse Problems for Acoustic, Electromagnetic and Elastic Wave Scattering," in Tomography and Inverse Problems, edited by D. C. Sabatico (Adam Hilger, Philadelphia, 1987).
9. A. C. Kak and M. Slaney, Principles of Computerized Tomographic Imaging, IEEE Press, New York (1988).
10. P. B. Abraham and C. F. Gaumond, "Reflection Tomography," Journal of Acoustical Society of America, Vol. 82, No. 4, p. 1303 (1987).
11. K. J. Langenberg, K. Mayer, T. Kreutter, V. Schmitz, "Computed Imaging with Elastic Waves," Proceedings of 12th World Conference on Nondestructive Testing, Amsterdam (April, 1989).